Controlled Generation of Single Microbubble at Solid Surfaces by a Nanosecond Pressure Pulse

Taehwa Lee,[1] Hyoung Won Baac,[2] Jong G. Ok,[1] Hong Seok Youn,[3] and L. Jay Guo[1,3,*,†]

[1]*Department of Mechanical Engineering, University of Michigan, Ann Arbor, Michigan 48109, USA*
[2]*School of Electronic and Electrical Engineering, Sungkyunkwan University, Suwon 440-746, Republic of Korea*
[3]*Department of Electrical Engineering and Computer Science, University of Michigan, Ann Arbor, Michigan 48109, USA*

(Received 9 April 2014; revised manuscript received 5 June 2014; published 22 August 2014)

We study the controlled generation of single microbubbles (approximately 100 μm) at solid surfaces in water. By focusing a nanosecond pressure pulse (<100 ns), the single microbubble is deterministically generated over the focal area, which is rather immune to surface heterogeneity that is typically responsible for uncontrolled bubble nucleation. Such controlled bubble nucleation is realized by strong negative pressure generated by pulsed optical excitation of a carbon-nanotube–polymer composite and its tight focusing (approximately 100 μm). The negative-pressure amplitude (>50 MPa), which is further increased by acoustic interference at an impedance-mismatched boundary, even exceeds the cavitation threshold of distilled water in a free-field (boundary-free) condition. This strong pressure can activate ubiquitous submicron nuclei in both water and surfaces, making the nucleation process controllable but irrelevant to a pit array (<10 μm in diameter). The ability to control bubble formation can lead to new applications in cell-level therapy, e.g., ablation of individual cancerous cells (microhistotripsy).

DOI: 10.1103/PhysRevApplied.2.024007

I. INTRODUCTION

Acoustically induced bubbles are extensively used in applications ranging from ultrasonic cleaning [1] and medical imaging and therapy to sonochemistry [2] because the radial collapse of bubbles and liquid jetting (resulting from symmetry breaking) can deliver spatially localized impacts [3]. In particular, bubble formation at solid surfaces has been increasingly important for selective surface modification for functional surfaces [4,5], nanocomposite formation [6], and single-bubble sonoluminescence [7]. Moreover, in the recent demonstration of laser-generated focused ultrasound that produces high-amplitude (>50 MPa) and high-frequency (>15 MHz) pressure with a small focal-spot size (<100 μm diameter) [8], acoustically induced microbubbles can disrupt single cancerous cells, thereby detaching them from the cultured substrate without affecting the neighboring cells [9]. This points to a new direction in histotripsy targeting at the cellular level. Such precise bubble localization can also allow the exploration of microscopic cell responses to high-frequency high-amplitude acoustic pressure, e.g., for drug delivery to individual cells [10]. In this regard, the reproducible generation of bubbles with high spatial accuracy represents a major interest and promising opportunity. However, the control of bubble nucleation at surfaces remains a challenging problem primarily because of surface heterogeneity that results in uncontrolled (or heterogeneous) bubble nucleation.

Heterogeneous bubble nucleation is the formation of gas bodies stabilized by nucleation sites such as impurities (e.g., hydrophobic particles) and cavities on the surface. The size and hydrophobicity of these nucleation sites determine the nucleation threshold, i.e., a critical tensile pressure required for the bubble nucleation. Thus, the bubble-formation process at solid surfaces is stochastic in nature and less controllable, relying on the distribution of the nucleation sites. Successful control of bubbles has been accomplished by either employing artificial nucleation sites, such as particles [11] and gas-filled pits [12,13], or by selectively controlling surface wettability [4].

On the other hand, focused ultrasound, which does not require surface modification or introduction of the bubble nuclei, is a promising modality for bubble generation, as it enables spatial localization of cavitation within a focal volume. High-intensity focused ultrasound has helped to realize this promise [14–19]. For example, minimally invasive targeted therapies have been demonstrated in histotripsy [17–19]. However, such approaches have typically used low frequencies that lead to a relatively large focal dimension (approximately mm), in which bubbles nucleate randomly or form a cloud of bubbles. Recently, Brujan and Matsumoto reported the generation of a single microbubble near a metal block by using multiple ultrasound pulses with dual-frequency components (approximately μs) [20]. However, such an approach is most likely

*Corresponding author.
†guo@umich.edu

dependent on surface quality; thus, it might produce different nucleation characteristics (less controllable) for other surfaces.

In this work, we demonstrate the controlled generation of single microbubbles at glass surfaces, irrespective of the influence of surface heterogeneity on the bubble-nucleation process. Surface-insensitive microbubble generation is made possible by highly localized negative pressure (negative focal-spot size of approximately 200 μm) with a single short pulse (<100 ns). Furthermore, due to the acoustic interference by the impedance boundary, the peak-negative-pressure amplitude (>50 MPa) exceeds the cavitation threshold of distilled water in a free-field (or boundary-free) condition (−33 MPa [21]). This approach enables single-microbubble nucleation in a controllable and reproducible manner, offering a new method to explore various interactions between acoustic bubbles and solid materials including biological objects such as cells and tissues.

II. EXPERIMENTAL SETUP

The experimental setup consists of an optoacoustic transmitter, a fiber-optic hydrophone, and an optical system for visualizing bubble nucleation, as illustrated in Fig. 1. Bubbles are nucleated on glass surfaces in a water tank filled with deionized water (Thermo Scientific, Barnstead GenPure Pro) at room temperature (20 °C). A flat cover glass (thickness 130–170 μm; VWR Scientific, Inc.) with surface roughness of 1–2 nm [22] is used for studying the bubble dynamics. The glass substrate is cleaned in an ultrasonic bath using acetone and isopropyl alcohol and then dried using nitrogen gas. In order to study the bubble nucleation at artificial nucleation sites, a microhole array (8 μm in diameter and 20 μm in spacing) is fabricated on the cover glass using photolithography followed by a deep-reactive-ion-etching process.

The optoacoustic wave is generated by pulsed optical excitation of a carbon-nanotube (CNT)–polymer composite layer coated on a concave lens (namely, optoacoustic lens [8]) as shown in Fig. 1(b). Here, for efficient optoacoustic conversion, the CNTs serve as an excellent light absorber and polydimethylsiloxane as a thermal expansion medium [23]. The acoustic wave from the optoacoustic lens (focal length approximately 5.5 mm) excited by a nanosecond Nd:YAG laser pulse (Continuum, Surelite I-20, $\lambda =$ 532 nm and pulse width = 6 ns) is focused onto a diffraction-limited spot. Because of acoustic diffraction [24], the original monopolar waveform (Gaussian temporal profile similar to that of the laser source) becomes a bipolar one (pulse width approximately 100 ns) at the focus, with a characteristic leading positive-compression phase followed by a trailing negative-tensile phase that is responsible for bubble inception. The acoustic signal and bubble nucleation are characterized by a broadband fiber-optic hydrophone (bandwidth up to 75 MHz). The hydrophone is also used to locate the acoustic focus.

Laser-induced acoustic waves and bubbles are visualized by laser-flash shadowgraphy [25]. This imaging technique

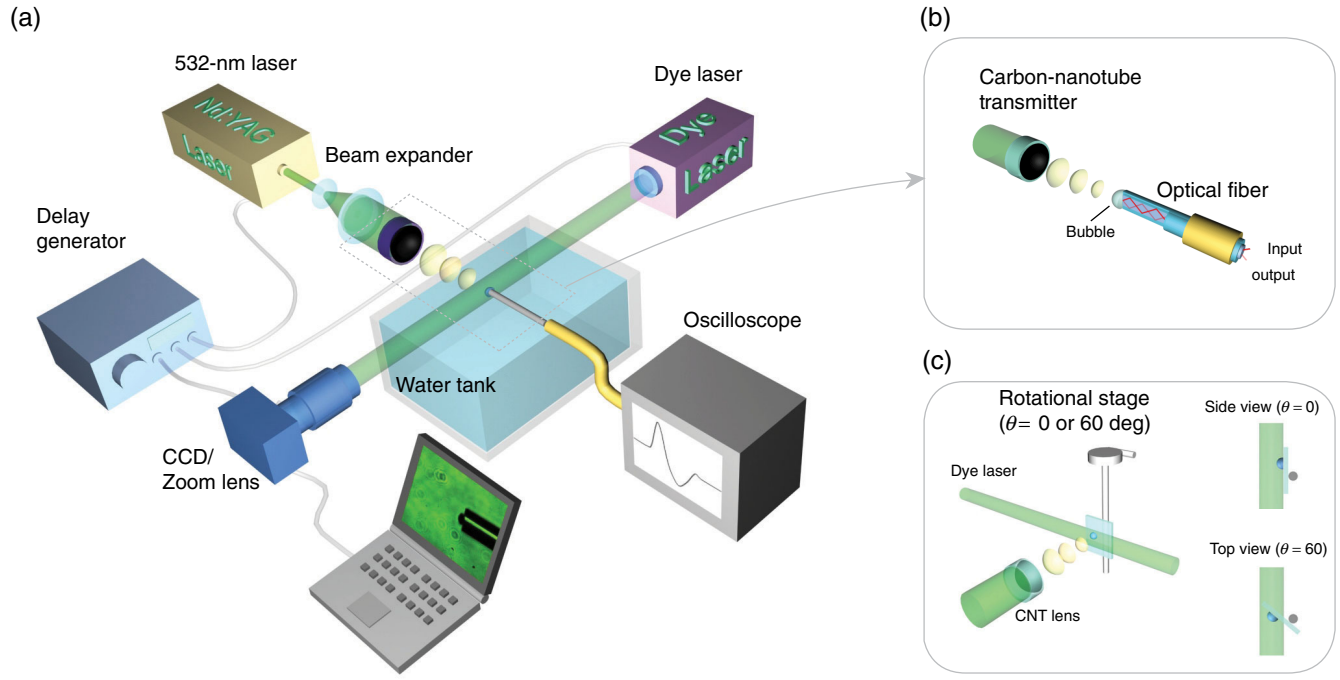

FIG. 1. (a) Acoustic-signal measurement with and without the bubble using a fiber-optic hydrophone. (b) The enlarged illustration of the fiber-optic-hydrophone measurement and the bubble. (c) Visualization of the bubble and acoustic wave by varying the angle of the glass substrate: side view ($\theta = 0°$), top view ($\theta = 60°$).

is a pump-probe method that allows a probe laser pulse (N_2-pumped dye laser, FWHM = 1 ns) to obtain shadow images of the bubbles at a different temporal moment specified by the time delay between the pump (Nd:YAG laser) and the probe pulses through a delay generator (Stanford Research Systems, DG535). Flat glass substrates mounted on a rotational stage are adjusted to obtain images in top view and side view, as shown in Fig. 1(c).

III. RESULT AND DISCUSSION

A. Pressure-field calculation and the effect of boundary reflection and interference

To study the bubble-nucleation process on a water-glass interface subject to a focused acoustic wave, we first examine acoustic interference due to wave reflection by the impedance boundary. The pressure field in the presence of the interface is substantially different from that in a free-field (boundary-free) condition, thereby having a significant effect on bubble nucleation [26]. To calculate the pressure field, the axisymmetric linear wave equation (in a lossless medium) is numerically solved using a finite-element method (the Courant number CFL < 0.05; COMSOL Multiphysics 4.3b). Since we focus on a diffraction-limited acoustic spot and the interference effect, the effects of nonlinearity and acoustic attenuation are assumed to be negligible for simplicity. First, the simulation is conducted in the absence of the acoustic reflector and compared with experimental results obtained in a free-field condition. With an appropriate choice of the initial conditions (i.e., initial acoustic pulse), the calculated signals at the focus can be well matched with the measured acoustic signals. Second, to see the interference effect, the reflector (acoustic reflectance $R = 0.8$) is then placed at the focus in the model by applying the impedance-boundary condition. Furthermore, the calculated pressure field due to interference (P_i) by axial-symmetric simulation is compared with those calculated by the one-dimensional (1D) reflection model, $P_i(z,t)_{1D}$, which can be represented by

$$P_i(z,t)_{1D} = f(t + z/c) + R \times f(t - z/c),$$

where $f(t)$, z, R, and c are the acoustic signal at the focus in a free-field condition, axial distance from the acoustic focal point ($z = 0$), acoustic reflectance, and speed of sound, respectively.

The peak-negative-pressure field near the glass substrate [$P_i(r,z)$, where r and z are the radial distance and axial distance from the acoustic focal point ($z = 0$, $r = 0$)] calculated by the axial-symmetric simulation is shown in Fig. 2(a). The amplitude of the pressure field is normalized to the maximum peak-negative-pressure amplitude in a free-field condition [the boundary-free peak negative pressure $P_f(r,z)$ has a maximum value at the focus, i.e., $P_f(r = 0, z = 0)$]. Indeed, the acoustic pressure field near the surface ($r < 50$ μm, $z < 50$ μm, the blue region) is

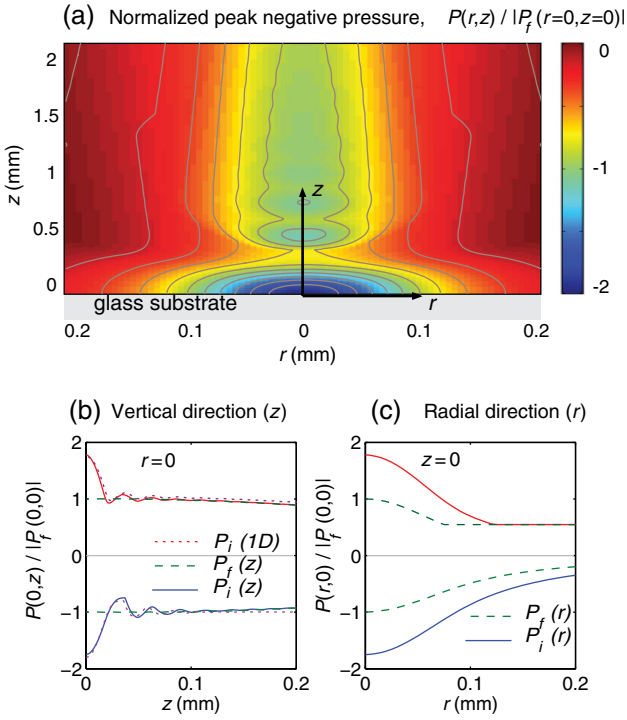

FIG. 2. (a) Calculated peak-negative-pressure field $P_i(r,z)$ near the glass surface (surface plot with contour lines) normalized to the maximum peak-negative-pressure amplitude in a free-field (or boundary-free) condition, $P_f(r = 0, z = 0)$. (b) Peak pressures in the z direction. The interfered pressure $P_i(z)$ is compared with the free-field pressure, $P_f(z)$. The interfered pressure based on a one-dimensional reflection model $P_i(1D)$ is also plotted for comparison. (c) Peak pressures in the r direction (Gaussian-like profile).

significantly enhanced by the flat reflector. Importantly, the pressure-enhanced blue region is closely related to the bubble-nucleation zones that were observed in the experiment. The peak-pressure distributions for the lateral (r) and axial (z) directions are shown in Figs. 2(b) and 2(c). The free-field pressure in the z direction $P_f(r = 0, z)$ remains constant within a range of z (<200 μm) because the upper limit is much less than the Rayleigh length (approximately $0.3z_R$) that is determined by using $z_R = \pi w_0^2/(c/f_c)$, where f_c, c, and w_0 are the center frequency of the measured acoustic signal (approximately 15 MHz), speed of sound in water, and acoustic spot size at the focus, respectively. The interference pressures at the interface $P_i(z = 0)$ are greatly increased up to 1.8 times ($P_i = P_f + RP_f = 1.8P_f$). The 1D reflection model, $P_i(z,t)_{1D}$, which does not consider wave diffraction, is in agreement with the axial-symmetric simulation results, indicating that the pressure augmentation near the interface can be understood as reflection and interference. Meanwhile, the interference pressure amplitudes decrease with r having a Gaussian-like profile $P(r) \sim \exp(-a \times r^2/w_0^2)$, as shown in Fig. 2(c).

By taking the interference effect into account, we can estimate optoacoustic-pressure amplitudes that are applied to the solid interfaces for bubble nucleation. Based on the free-field (or boundary-free) pressure amplitudes previously reported [8], the maximum positive pressure at the interface can be estimated as +100 MPa ($1.8P_{f+}$) and the negative pressure as −50 MPa ($1.8P_{f-}$). The negative pressures have even higher amplitudes than the acoustic cavitation threshold of distilled water in a free-field condition ($P_{\text{th,water}} \sim -33$ MPa [21]).

B. Bubble-dynamics modeling

The bubbles are apparently formed within the duration of the short acoustic pulse (further discussion will follow). Thus, the initial stages of bubble growth are dominated by inertia due to their high rarefaction stress and short duration. The radius of isolated bubbles (R) is calculated by using the Rayleigh-Plesset equation assuming spherical symmetry and an adiabatic gas law [27,28]

$$R\ddot{R} + \frac{3}{2}\dot{R}^2 = \frac{1}{\rho}\left\{\left(p_0 + \frac{2\sigma}{R_0} - p_v\right)\left(\frac{R_0}{R}\right)^{3\gamma} + p_v - \frac{2\sigma}{R} - \frac{4\eta\dot{R}}{R} - p_0 - P(t)\right\},$$

where R, R_0, ρ, σ, η, p_v, p_0, and $P(t)$ are the bubble radius, initial bubble radius, density ($\rho = 1000$ kg m^{-3}), coefficient of surface tension ($\sigma = 0.073$ N m^{-1}), water viscosity ($\eta = 1.0 \times 10^{-3}$ Pa s), water-vapor pressure, static ambient pressure, and applied acoustic pressure, respectively. In the experiment, the acoustic pulse duration (<100 ns) is 2 orders of magnitude shorter than the measured bubble lifetime. After the bubbles' nucleation, the rest of the bubble dynamics is driven by inertia under static ambient pressure [29]. The initial bubble radius (R_0) is chosen by a condition that for a given pressure (−20 MPa), the bubble expansion is minimal below a certain value for R, whereas above this value, much greater bubble growth is observed.

Figure 3(a) shows the calculated bubble radii for different negative pressures with an initial radius of 5 nm. With the short pressure pulses applied, the bubbles explosively grow and subsequently shrink (symmetric behavior). The maximum bubble radius increases with the negative-pressure amplitude. The ratio of the maximum radius to the initial radius ($R_{\max}/R_0$) is calculated to be over 100. Moreover, the bubble lifetime is calculated to be much longer than the acoustic pulse duration. The velocity of the bubble wall reaches as high as 100 m/s, as shown in Fig. 3(b). Here, our calculation is limited to the isolated free-boundary bubbles. In the experiment, densely packed bubbles nucleated at solid surfaces interact with one another. A more rigorous theoretical analysis of bubble nucleation on solid surfaces can be found elsewhere [13,30]. Furthermore, bubble-to-bubble interaction and coalescence are discussed in the literature [12,31].

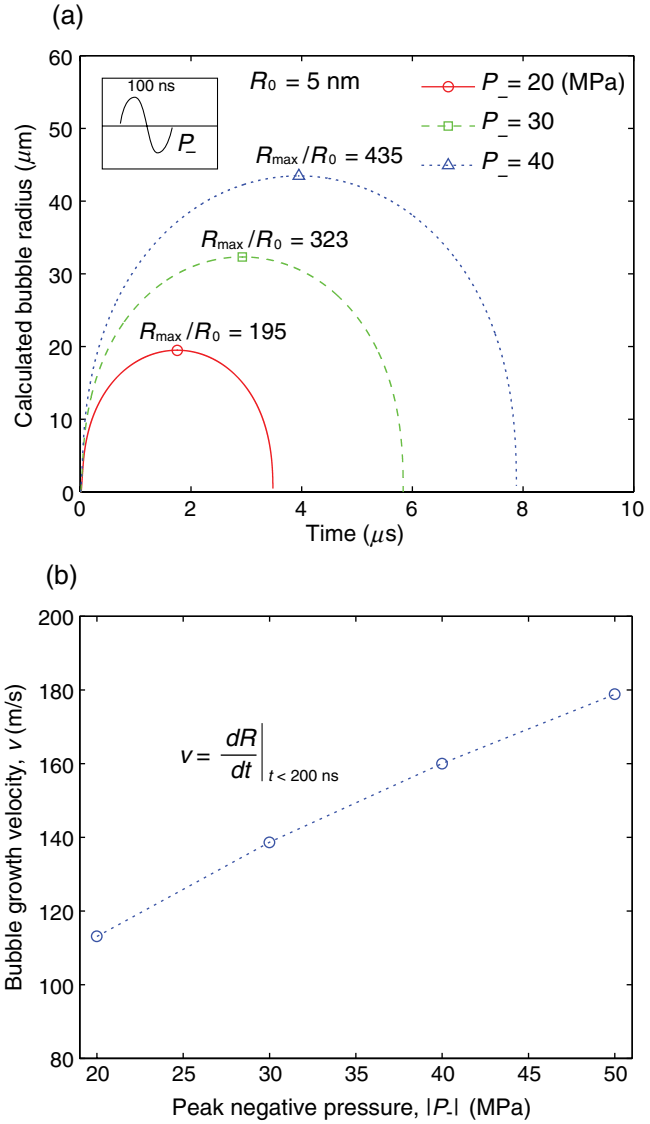

FIG. 3. (a) Calculated dynamics of isolated single bubbles for negative pressures ($P_- = 20$, 30, 40 MPa). (b) The velocity of seed bubble growth at an early time ($t < 200$ ns).

C. Characterization of bubble dynamics: Nucleation, growth, and collapse

Single-microbubble generation visualized by laser-flash shadowgraphy is summarized in Fig. 4 for laser energy of 36 mJ/pulse (approximately −41 MPa). Figure 4(a) shows bubble dynamics at the glass interface (side view, $\theta = 0°$). The acoustic wave front (A_{inc}) generated by the optoacoustic lens is first captured before bubble nucleation ($t = -100$ ns). The reflected wave (A_{ref}) is observed ($t = 100$ ns), followed by the primary shock wave (S1) induced by the explosive bubble growth (Fig. 3). At a delay time of 1 μs, a thin bubble layer is formed at the surface,

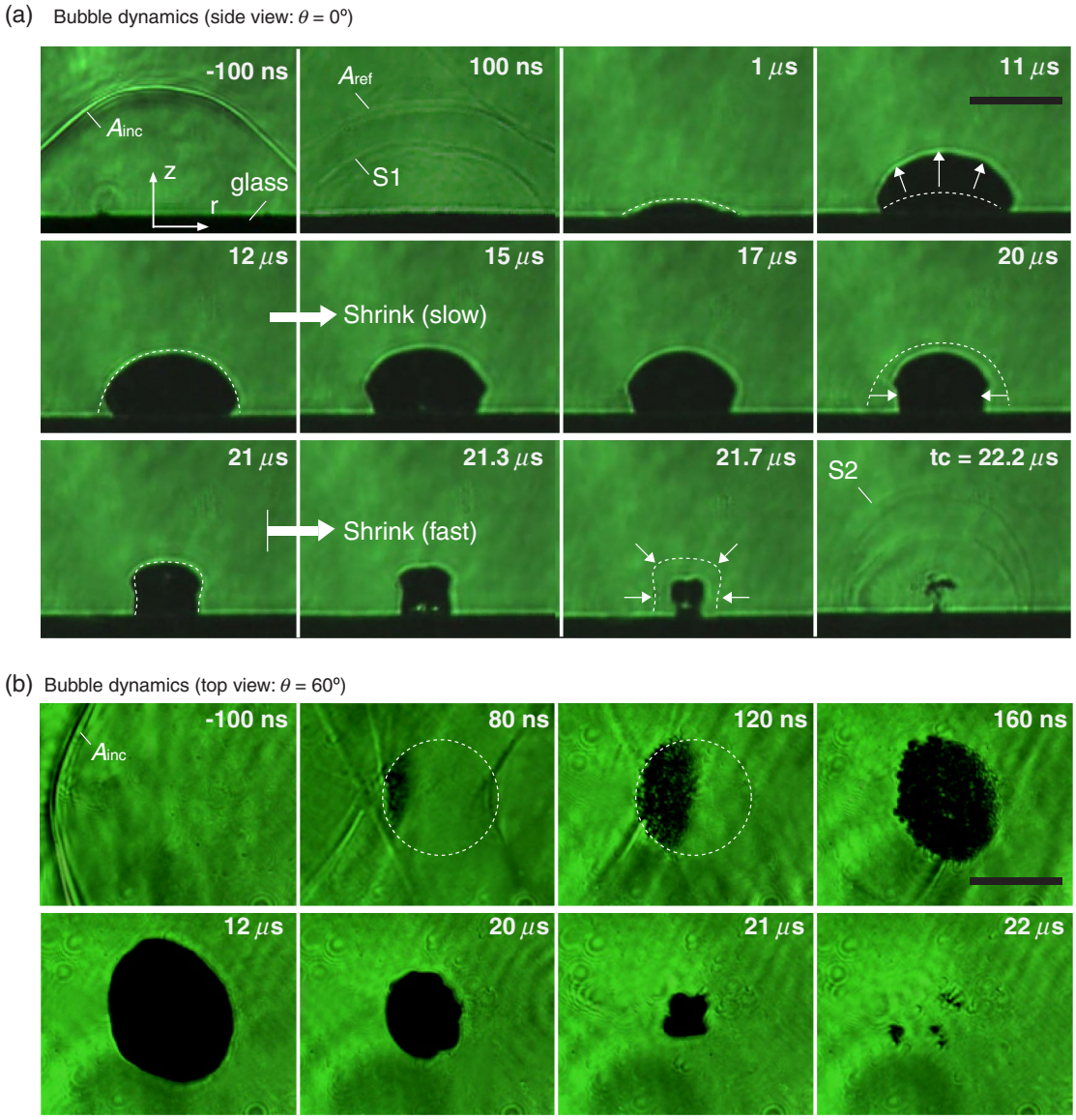

FIG. 4. (a) Shadowgraph images of focused acoustic wave and bubble nucleation at the laser energy of 36 mJ/pulse (approximately $1.8E_w$). The single optoacoustic pulses (A_{inc}) are targeted on the flat glass surface. The reflected wave (A_{ref}) followed by the primary shock wave (S1) is observed ($t = 100$ ns). The dashed lines are drawn for comparison. (b) Top-view images in an early stage of bubble nucleation at the glass surface. The surface is slightly tilted with respect to the vertical axis. The circular dashed line represents a nucleation zone. The bar indicates a length of 100 μm.

and its shape closely matches the blue region of the simulated peak-pressure field in Fig. 2(a). The bubble preferentially grows upward and reaches the maximum size ($t = 11$ μs) and then it starts to shrink. Interestingly, the shrinkage of the bubble takes place in two stages: slow and fast shrinkages. In the slow-shrinkage stage, the height of the bubble is nearly constant, while the side walls of the bubble cave in over a relatively long time (from 12 to 20 μs), evolving into a "mushroom" shape. This slow-shrinkage process is followed by the fast one, in which the radial collapse of the bubble starts ($t = 21.7$ μs), producing a cavitation shockwave (S2, $t = 22.2$ μs). Since the acoustic bubble here evolves from the thin bubble layer at the interface, the bubble dynamics exhibits similarity with those induced by the laser excitation of a thin absorbing liquid layer in contact with a glass substrate [32].

The early stage of the bubble nucleation is shown in Fig. 4(b) for a top view ($\theta = 60°$). Closely spaced small bubbles start to appear on the left edge of the circular zone (dashed circle) at the glass surface (at $t = 80$ ns). Note that the glass substrate is tilted with respect to the vertical axis ($\theta = 60°$); thus, the left half of the glass is closer to the CNT lens, as illustrated in Fig. 1(c). Although some seed bubbles are observed at the edge of the circular area, the dense bubbles form a thin layer covering most of the focal area (approximately 100 μm) on the glass surface

(by $t = 160$ ns). The individual seed bubbles are rarely identified after 1 μs, as they grow and coalesce into a single large bubble exhibiting a defined bubble edge in the images. The coalescence of bubbles observed in this experiment stands in sharp contrast to conventional approaches, in which many bubbles form a cloud of bubbles, each remaining separately [33].

Merged bubble radii with respect to time are plotted in Fig. 5(a) for different laser energies ($E = 14$, 19, 22, 39, 51 mJ/pulse). By assuming hemispherical bubbles, the bubble radius is calculated from the bubble area in the side-view shadowgraph images. The maximum bubble radius and lifetime increase with increasing laser energies. Characteristic times as a function of the maximum bubble radius are shown in Fig. 5(b) for bubble collapse (t_c) and bubble lifetime (t_l). The Rayleigh collapse time (t_R) [34] is plotted for comparison (dotted line). The bubble lifetime (t_l) is more than 2 times longer than the bubble collapse time (t_c), indicating that the bubble shrinkage proceeds faster than its expansion. This might be due to the bubble-bubble interaction and their merging during the bubble growth [11]. Note that the collapse time is even shorter than the Rayleigh collapse time. This discrepancy is because the Rayleigh collapse is defined to describe the symmetric motion of a spherical bubble in an infinite liquid, rather than the asymmetric one shown in our case.

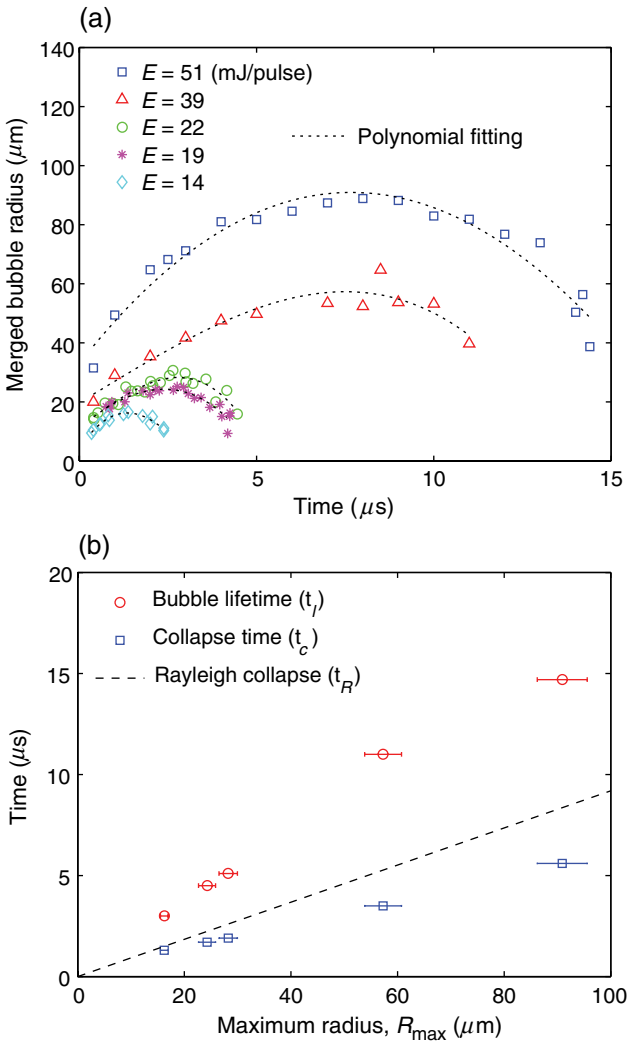

FIG. 5. (a) Merged bubble radius as a function of time for laser energies ($E = 14$, 19, 22, 39, 51 mJ/pulse) and third-order polynomial fit lines. (b) Characteristic times of bubble dynamics: bubble lifetime (t_l), collapse time (t_c), and Rayleigh collapse time (t_R).

The bubble coalescence behavior on the solid boundary is further investigated by monitoring the hydrophone signals. Figure 6(a) shows the measured acoustic signals for different laser energies ($E = 14$, 19, 22 mJ/pulse). The measured signals exhibit different characteristics depending on the presence of bubbles at the tip of the hydrophone, as shown in the inset of Fig. 6(a). Without bubbles, the hydrophone detects a single bipolar acoustic pulse (<100 ns pulse duration). However, with bubbles, the hydrophone cannot capture full (positive and negative) acoustic signals because the negative signals are distorted by the bubbles, which can significantly increase negative signal amplitudes due to a large refractive-index contrast between the vapor bubble and the hydrophone tip. Instead, the negative signals contain useful information on bubble dynamics. First, the rapid increase in the negative

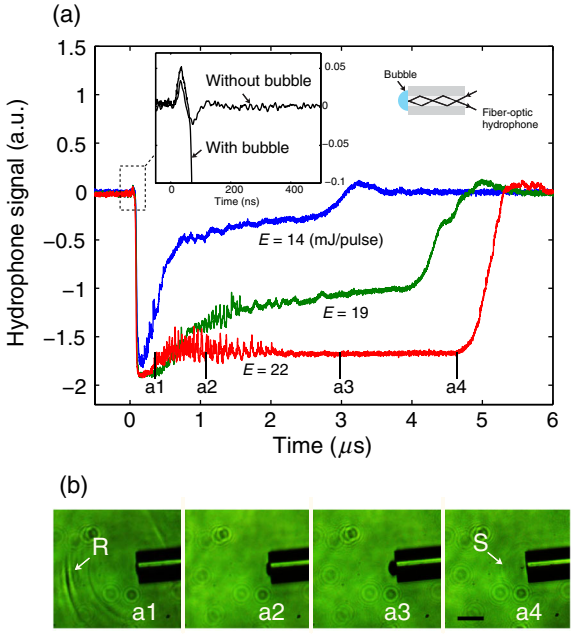

FIG. 6. (a) The hydrophone signals for laser energies ($E = 14$, 19, 22 mJ/pulse). The temporal durations of the signals corresponded to the bubble lifetimes. The inset shows the difference between the signals with and without bubbles at the tip of the hydrophone. (b) The shadowgraph images of bubbles at the tip of the fiber-optic hydrophone (6-μm core and 125-μm cladding diameter) at a laser energy of 22 mJ/pulse ($1.6E_{th}$) for correlating the measured acoustic signal. The arrows indicate the reflected wave (R) and shock wave (S). The bar indicates a length of 100 μm.

amplitude reveals that the bubble starts to expand rapidly within the acoustic pulse duration as short as $t < 100$ ns. Second, the temporal duration of the signal corresponds to the bubble lifetime. Once the negative amplitude reaches its maximum value, it then decays over a relatively long period on the order of several μs. The signal eventually returns to a positive value after the bubble collapse. Third, the negative signals show a signature of the merging process of individual microbubbles. By correlating the measured hydrophone signals ($E = 22$ mJ/pulse) with time-resolved images [a1–a4 in Fig. 6(b)], we confirm that during bubble merging, the signals are highly oscillatory (0.1–2 μs). After bubble merging, the hydrophone signals become relatively stable over a longer time (>2 μs), because the single merged bubbles completely cover the sensing zone on the fiber tip (6-μm core and 125-μm cladding diameter).

D. Bubble generation on flat surface and on surface with microstructures

The single bubble that forms through the coalescing of grown seed bubbles is found to be rather immune to surface quality. To demonstrate this, a control experiment is conducted using two different surfaces: a smooth-glass substrate (surface roughness of 1–2 nm [22]) and a glass substrate patterned with a microhole array [8 μm in diameter and 20 μm in spacing; see the microscope image in Fig. 7(c)]. We anticipate that the nucleation threshold amplitude (P_{th}) will decrease by the microstructures on the glass substrate because the bubble-nucleation threshold strongly depends on the size of the nucleation sites based on the crevice model [30]. The bubble-nucleation threshold on the patterned glass with the microstructures referred to as $P_{th,micro}$ is measured to be -14.3 MPa, while the threshold on the smooth glass is -24 MPa, which we will refer to as $P_{th,nano}$ because bubbles can nucleate at the nanoscale nucleation sites both in water and on the surfaces (note that $P_{th,nano}$ is different from $P_{th,water}$ determined by nucleation sites only in water). As bubble nucleation is a statistical event, the cavitation probability (P_{cav}) transits from 0 to 1 by increasing negative-pressure amplitudes [35,36]. Accordingly, we define the nucleation thresholds as the minimum negative-pressure amplitude at which cavitation occurs repeatedly and controllably with the cavitation probability close to 1 ($P_{cav} \sim 1$). Although bubbles nucleate at the solid surface, the measured nucleation threshold without the micropatterns ($P_{th,nano}$) has relatively high amplitude, even approaching the bubble-nucleation thresholds in a free-field (or boundary-free) condition ($P_{th,water}$ ranges from -24 to -33 MPa from multiple independent measurements [21,35,37]). This is because the glass samples used are very smooth (surface roughness of 1–2 nm) and hydrophilic. Furthermore, the nucleation threshold with the micropatterns ($P_{th,micro}$) also have a relatively high amplitude and may be determined by the bottom surface of the patterned holes roughened due to the dry-etching process.

Figures 7(a)–7(c), lower panel, show the bubble nucleation for two different glass surfaces. Depending on the pressure amplitudes, the bubble nucleation exhibits different characteristics: in weak negative pressures, bubbles

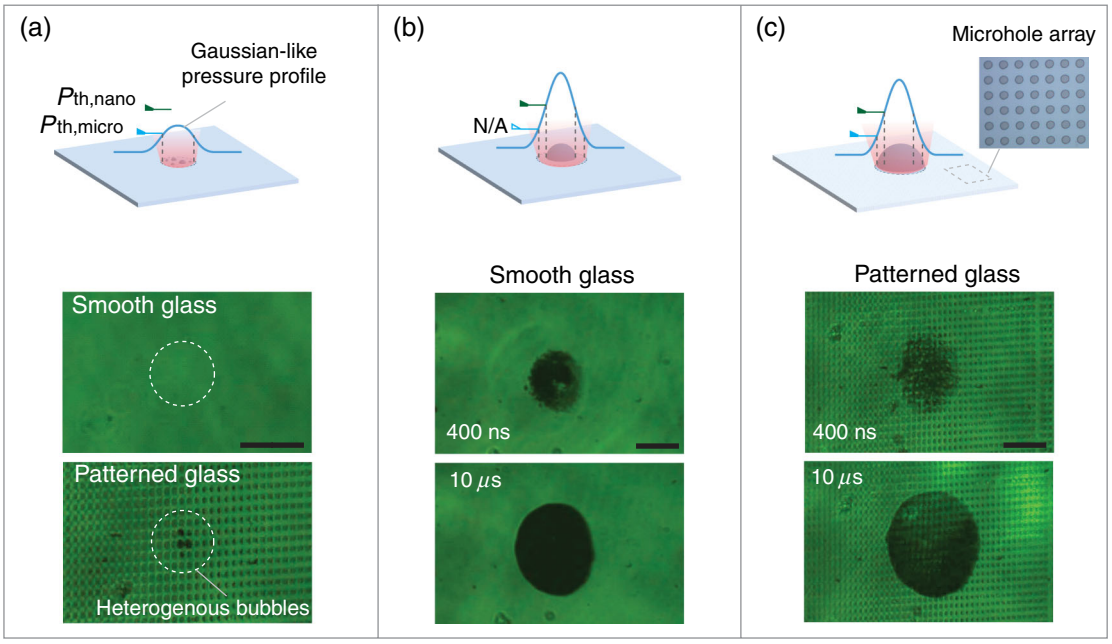

FIG. 7. (a) At low negative-pressure amplitudes ($|P_{th,micro}| < P_- < |P_{th,nano}|$), heterogeneous bubble nucleation on the patterned glass ($P_{th,nano} = -24$ MPa, $P_- = 16$ MPa, $P_{th,micro} = -14.3$ MPa). At high negative-pressure amplitudes ($P_- \gg |P_{th,nano}|$, $P_- = \sim 44.8$ MPa), controlled microbubbles on the smooth glass (b) and on the patterned glass (c). The inset of (c) shows the microscope image of the glass patterned with a microhole array (8 μm in diameter, 20 μm in spacing). The bar indicates a length of 100 μm.

nucleate preferentially at the microholes, whereas strong negative pressures make the microstructure irrelevant, generating a large merged bubble. Specifically, when the negative-pressure amplitudes are slightly higher than the nucleation threshold of the glass substrate with the microholes but less than the threshold of the smooth glass ($|P_{\text{th,micro}}| < P_- < |P_{\text{th,nano}}|$), a few microbubbles ($<10\,\mu$m) nucleate only at the microholes on the patterned glass, as shown in Fig. 7(a) for $P_- = 16$ MPa. The observed bubbles are typically characteristic of heterogeneous bubble nucleation (thus, we will refer to the zone as a "heterogeneous" nucleation zone and its diameter as d_H). In contrast, at strong negative pressures ($P_- = 44.8$ MPa $> |P_{\text{th,micro}}|$), the glasses with and without the microholes show no qualitative difference in the bubble-nucleation process. As shown in Figs. 7(b) and 7(c), the densely packed tiny bubbles ($t = 400$ ns) are merged into a single large bubble (approximately 100 μm) at a later time ($t = 10\,\mu$s). However, the bubble zone and the merged bubble are slightly increased by the microholes [Fig. 7(c)].

Bubble-nucleation characteristics can be categorized by three regimes: heterogeneous regime, mixed regime, and controlled regime, as illustrated in Fig. 8 for large and small acoustic spot sizes. In the heterogeneous regime, where peak-negative-pressure amplitudes are higher than $|P_{\text{th,micro}}|$ but lower than $|P_{\text{th,nano}}|$, bubbles nucleate preferentially. In the mixed regime ($P_- > |P_{\text{th,nano}}|$), a small controlled region is surrounded by a large heterogeneous region (i.e., low d_C/d_H). In this regime, even with a large acoustic spot, a small controlled bubble ($d_C \sim 100\ \mu$m) can be produced, but a much larger heterogeneous bubble zone is unavoidable due to potential surface heterogeneity (or lower nucleation threshold). By further increasing negative-pressure amplitudes, the characteristics of bubble nucleation fall into the controlled regime where densely populated bubbles nucleate and subsequently coalesce, forming a single large bubble. In the controlled regime ($P_- \gg |P_{\text{th,nano}}|$) with high d_C/d_H, the size of the merged bubble approaches the acoustic spot size (w_0), and with a large acoustic spot, large controlled bubbles nucleate. Thus, a controlled microbubble (approximately 100 μm) requires not only a small acoustic spot but also high pressure amplitudes.

The bubble-nucleation zones can be increased by either increasing the applied negative-pressure amplitudes or by decreasing the nucleation threshold. From the simulation [Fig. 4(c)], the focused pressure field has an axial-symmetric Gaussian-like profile, $P(r) = P_- \exp(-a \times r^2/w_0^2)$ where P_- and w_0 are the peak negative amplitude at the focus and the acoustic spot size (FWHM), respectively; the a should be $4\ln(2)$ to satisfy $P(r = w_0/2) = P_-/2$. We can quantify the nucleation zones (d_{zone}) by equating the pressure amplitudes at the zone edge to the nucleation thresholds, i.e., $P(r = d_{\text{zone}}/2) = P_{\text{th}}$:

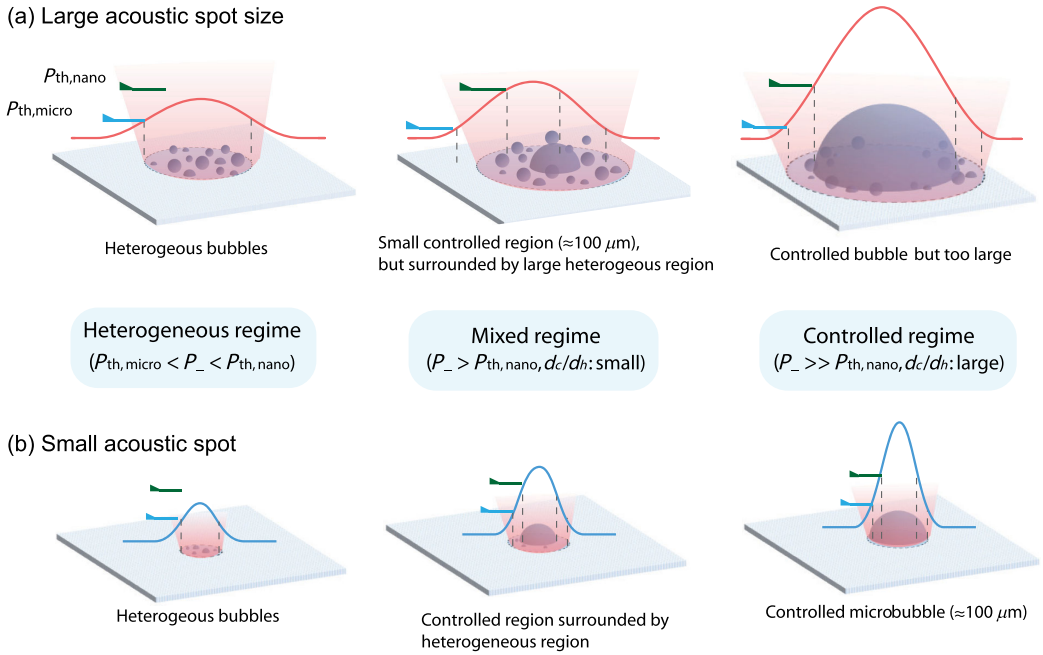

FIG. 8. Bubble-nucleation characteristics categorized by three regimes for a large acoustic spot (a) and a small acoustic spot (b): heterogeneous regime ($|P_{\text{th,micro}}| < P_- < |P_{\text{th,nano}}|$), mixed regime ($P_- > |P_{\text{th,nano}}|$), and controlled regime ($P_- \gg |P_{\text{th,nano}}|$). (a) For a large acoustic spot, a small controlled region (approximately 100 μm) can be produced in the mixed regime, but it is surrounded by a large heterogeneous region. By further increasing the pressure amplitudes (controlled regime), controlled bubbles nucleate but they are too large (close to the acoustic spot size, w_0). (b) For a small spot size, microbubbles nucleate in the controlled regime.

$$P(r = d_{\text{zone}}/2) = P_{\text{th}} = P_{-}\exp[-\ln(2) \times {d_{\text{zone}}}^2/w_0^2].$$

Then the nucleation zones can be estimated as

$$d_{\text{zone}} = w_0\sqrt{\ln(P_{-}/P_{\text{th}})/\ln(2)} \sim 1.2w_0\sqrt{\ln(P_{-}/P_{\text{th}})},$$

which is a function of nucleation threshold (P_{th}), maximum peak negative pressure (P_{-}), and acoustic spot size (w_0). By inspection, the nucleation zone increases with increasing w_0 and with increasing the peak-pressure amplitude, P_{-}, while it decreases with P_{th}. Figure 9 shows the estimated nucleation zones for two different acoustic spot sizes ($w_0 = 200$ and 500 μm). The controlled zones (d_C, solid line) and heterogeneous zones (d_H, dotted line) are calculated with two nucleation thresholds, $P_{\text{th,nano}}$ (−24 MPa) and $P_{\text{th,micro}}$ (−14 MPa), respectively. Regardless of the acoustic spot size (w_0), the calculated nucleation zones increase with P_{-}; the controlled zones are larger than the heterogeneous zones. Moreover, the ratio of the zones (d_C/d_H, dashed line) increases with P_{-}. The ratio d_C/d_H can be a measure of whether the bubble nucleation is controllable or not. The higher the zone ratio, the closer the overall characteristic of the bubble nucleation approaches the controlled nucleation. The shaded regions indicate pressure ranges that correspond to controlled bubble zones (d_C) with a diameter of approximately 100 μm. For the large spot ($w_0 = 500$ μm), the shaded region is very narrow, indicating that the controlled zones with approximately 100 μm diameter are allowed only at the near-threshold pressures (approximately $P_{\text{th,nano}}$) where the ratio d_C/d_H is small (i.e., mixed regime). However, for the small spot ($w_0 = 200$ μm), the shaded region covers a wide range of pressures that fit into the controlled regime with high ratio d_C/d_H and controlled microbubble (100 μm).

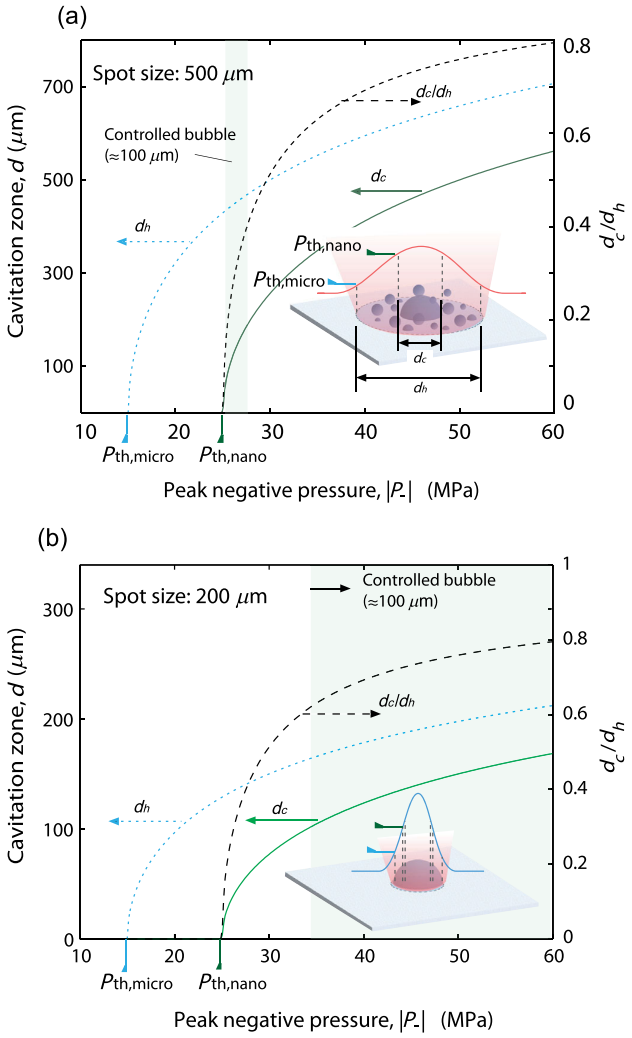

FIG. 9. Calculated cavitation zones for nucleation thresholds ($P_{\text{th,nano}} = -24$ MPa, $P_{\text{th,micro}} = -14$ MPa) for a large spot size ($w_0 = 500$ μm) (a) and for a small spot size ($w_0 = 200$ μm) (b). Controlled bubble zone (d_c) for $P_{\text{th,nano}}$, heterogeneous bubble zone (d_h) for $P_{\text{th,micro}}$. The shaded regions indicate a range of pressures that can produce controlled bubbles of approximately 100 μm.

IV. SUMMARY

We demonstrate and analyze the controlled generation of a single microbubble at solid surfaces. Our approach enables a tight confinement of a single merged microbubble with microscale accuracy, regardless of surface-induced heterogeneity. The ability to control bubble formation can lead to new applications, for example, ablation of individual cancerous cells (microhistotripsy) and precise cell sonoporation or disruption [9,38] and selective surface modification.

ACKNOWLEDGMENT

This work is supported in part by NSF Grant No. DMR 1120187.

[1] M. O. Lamminen, H. W. Walker, and L. K. Weavers, Mechanisms and factors influencing the ultrasonic cleaning of particle-fouled ceramic membranes, J. Membr. Sci. **237**, 213 (2004).
[2] K. S. Suslick, Sonochemistry, Science **247**, 1439 (1990).
[3] E. B. Flint and K. S. Suslick, The temperature of cavitation, Science **253**, 1397 (1991).
[4] V. Belova, D. A. Gorin, D. G. Shchukin, and H. Mohwald, Selective ultrasonic cavitation on patterned hydrophobic surfaces, Angew. Chem., Int. Ed. **49**, 7129 (2010).
[5] D. G. Shchukin, E. Skorb, V. Belova, and H. Moehwald, Ultrasonic cavitation at solid surfaces, Adv. Mater. **23**, 1922 (2011).
[6] V. Belova, T. Borodina, H. Mohwald, and D. G. Shchukin, The effect of high intensity ultrasound on the loading of Au nanoparticles into titanium dioxide, Ultrason. Sonochem. **18**, 310 (2011).

[7] D. F. Rivas, A. Prosperetti, A. G. Zijlstra, D. Lohse, and H. J. G. E. Gardeniers, Efficient sonochemistry through microbubbles generated with micromachined surfaces, Angew. Chem., Int. Ed. **49**, 9699 (2010).

[8] H. W. Baac, J. G. Ok, A. Maxwell, K. T. Lee, Y. C. Chen, A. J. Hart, Z. Xu, E. Yoon, and L. J. Guo, Carbon-nanotube optoacoustic lens for focused ultrasound generation and high-precision targeted therapy, Sci. Rep. **2**, 989 (2012).

[9] H. W. Baac, J. Frampton, J. G. Ok, S. Takayama, and L. J. Guo, Localized micro-scale disruption of cells using laser-generated focused ultrasound, J. Biophoton., **6**, 905 (2013).

[10] P. Prentice, A. Cuschierp, K. Dholakia, M. Prausnitz, and P. Campbell, Membrane disruption by optically controlled microbubble cavitation, Nat. Phys. **1**, 107 (2005).

[11] M. Arora, C. D. Ohl, and D. Lohse, Effect of nuclei concentration on cavitation cluster dynamics, J. Acoust. Soc. Am. **121**, 3432 (2007).

[12] N. Bremond, M. Arora, C. D. Ohl, and D. Lohse, Controlled multibubble surface cavitation, Phys. Rev. Lett. **96**, 224501 (2006).

[13] B. M. Borkent, S. Gekle, A. Prosperetti, and D. Lohse, Nucleation threshold and deactivation mechanisms of nanoscopic cavitation nuclei, Phys. Fluids **21**, 102003 (2009).

[14] C. C. Coussios and R. A. Roy, Applications of acoustics and cavitation to noninvasive therapy and drug delivery, Annu. Rev. Fluid Mech. **40**, 395 (2008).

[15] C. C. Coussios, C. H. Farny, G. Ter Haar, and R. A. Roy, Role of acoustic cavitation in the delivery and monitoring of cancer treatment by high-intensity focused ultrasound (HIFU), International Journal of Hyperthermia **23**, 105 (2007).

[16] B. A. Rabkin, V. Zderic, and S. Vaezy, Hyperecho in ultrasound images of HIFU therapy: Involvement of cavitation, Ultrasound Med. Biol. **31**, 947 (2005).

[17] W. W. Roberts, T. L. Hall, K. Ives, J. S. Wolf, J. B. Fowlkes, and C. A. Cain, Pulsed cavitational ultrasound: A noninvasive technology for controlled tissue ablation (histotripsy) in the rabbit kidney, J. Urol. **175**, 734 (2006).

[18] Z. Xu, M. Raghavan, T. L. Hall, C. W. Chang, M. A. Mycek, J. B. Fowlkes, and C. A. Cain, High speed imaging of bubble clouds generated in pulsed ultrasound cavitational therapy-histotripsy, IEEE Trans. Ultrason. Ferroelectr. Freq. Control **54**, 2091 (2007).

[19] A. D. Maxwell, C. A. Cain, A. P. Duryea, L. Q. Yuan, H. S. Gurm, and Z. Xu, Noninvasive thrombolysis using pulsed ultrasound cavitation therapy—histotripsy, Ultrasound Med. Biol. **35**, 1982 (2009).

[20] E.-A. Brujan and Y. Matsumoto, Collapse of micrometer-sized cavitation bubbles near a rigid boundary, Microfluid. Nanofluid. **13**, 957 (2012).

[21] G. N. Sankin and V. S. Teslenko, Two-threshold cavitation regime, Dokl. Phys. **48**,665 (2003).

[22] A. L. Sumner, E. J. Menke, Y. Dubowski, J. T. Newberg, R. M. Penner, J. C. Hemminger, L. M. Wingen, T. Brauers, and B. J. Finlayson-Pitts, The nature of water on surfaces of laboratory systems and implications for heterogeneous chemistry in the troposphere, Phys. Chem. Chem. Phys. **6**, 604 (2004).

[23] H. W. Baac, J. G. Ok, H. J. Park, T. Ling, S. L. Chen, A. J. Hart, and L. J. Guo, Carbon nanotube composite optoacoustic transmitters for strong and high frequency ultrasound generation, Appl. Phys. Lett. **97**, 234104 (2010).

[24] G. J. Diebold, T. Sun, and M. I. Khan, Photoacoustic monopole radiation in 1-dimension, 2-dimension, and 3-dimension, Phys. Rev. Lett. **67**, 3384 (1991).

[25] X. Zeng, X. L. Mao, R. Greif, and R. E. Russo, Experimental investigation of ablation efficiency and plasma expansion during femtosecond and nanosecond laser ablation of silicon, Appl. Phys. A **80**, 237 (2005).

[26] M. L. Calvisi, J. I. Iloreta, and A. J. Szeri, Dynamics of bubbles near a rigid surface subjected to a lithotripter shock wave. Part 2. Reflected shock intensifies non-spherical cavitation collapse, J. Fluid Mech. **616**, 63 (2008).

[27] C. E. Brennen, *Cavitation and Bubble Dynamics* (Oxford University Press, New York, 1995).

[28] J. D. Bernardin and I. Mudawar, A cavity activation and bubble growth model of the Leidenfrost point, J. Heat Transfer **124**, 864 (2002).

[29] H. G. Flynn, Cavitation dynamics. 2. Free pulsations and models for cavitation bubbles, J. Acoust. Soc. Am. **58**, 1160 (1975).

[30] A. A. Atchley and A. Prosperetti, The crevice model of bubble nucleation, J. Acoust. Soc. Am. **86**, 1065 (1989).

[31] N. Bremond, M. Arora, S. M. Dammer, and D. Lohse, Interaction of cavitation bubbles on a wall, Phys. Fluids **18**, 121505 (2006).

[32] T. Lee, D. Jang, D. Ahn, and D. Kim, Effect of liquid environment on laser-induced backside wet etching of fused silica, J. Appl. Phys. **107**, 033112 (2010).

[33] H. Chen, X. J. Li, M. X. Wan, and S. P. Wang, High-speed observation of cavitation bubble clouds near a tissue boundary in high-intensity focused ultrasound fields, Ultrasonics **49**, 289 (2009).

[34] Lord Rayleigh, On the pressure developed in a liquid during the collapse of a spherical cavity, Philos. Mag. **34**, 94 (1917).

[35] A. D. Maxwell, C. A. Cain, T. L. Hall, J. B. Fowlkes, and Z. Xu, Probability of cavitation for single ultrasound pulses applied to tissues and tissue-mimicking materials, Ultrasound Med. Biol. **39**, 449 (2013).

[36] F. Caupin and E. Herbert, Cavitation in water: A review, C.R. Phys. **7**, 1000 (2006).

[37] B. M. Borkent, M. Arora, and C. D. Ohl, Reproducible cavitation activity in water-particle suspensions, J. Acoust. Soc. Am. **121**, 1406 (2007).

[38] H. W. Baac, T. Lee, and L. J. Guo, Micro-ultrasonic cleaving of cell clusters by laser-generated focused ultrasound and its mechanisms, Biomed. Opt. Express **4**, 1442 (2013).